Appl. Phys. B (2017) 123:79
DOI 10.1007/s00340-017-6641-y

Applied Physics B
Lasers and Optics

Practical correction of a phase-aberrated laser beam using a triphenyldiamine-based photorefractive composite

Yichen Liang[1] · Jeffrey G. Winiarz[1]

Received: 23 May 2016 / Accepted: 12 January 2017 / Published online: 3 March 2017

Abstract A photorefractive composite based on a triphenyldiamine (TPD) derivative was used to restore a severely phase-aberrated laser beam to a nearly aberration-free state. Here, a forward degenerate four-wave mixing geometry was employed for the elimination of phase distortions and its practical applicability in the transmission of optically encoded data is demonstrated. In addition, it is demonstrated that the experimental geometry is able to effectively restore dynamically updating images. Conventional two-beam coupling and degenerate four-wave mixing experiments were used to characterize the composite subject to the current experimental setup. The two-beam coupling net gain coefficient was 100 cm^{-1} with an applied external electric field of 70 V/μm. Internal and external diffraction efficiencies of 10 and 6%, respectively, were observed with a similar external electric field. Due to its superior charge-carrier mobility, the TPD-based composite exhibited a response time of 0.28 s, approximately five times faster than traditional PVK-based composites.

1 Introduction

Research in optical communications progressed swiftly in the late 20th century due to rapid advancements in laser technology. Unfortunately, aberrations arising from imperfections in the transmission media (e.g., atmosphere, optical fiber, etc) pose a critical issue, because they lead to degradation of the transmitted signal. Several techniques involving adaptive optics have been developed to address this issue [1, 2]. These techniques, however, are costly and require complicated electronics. In contrast, holographic techniques using photorefractive (PR) elements offer a simple approach and are relatively cost effective [3–5]. Previous research has demonstrated that, due to the absence of phase cross talk between the two writing beams, inorganic PR crystals can be used for the elimination of phase aberrations using two-wave mixing [6, 7]. In contrast, organic PR composites provide an attractive alternative to inorganic crystals due to their low cost, ease of processability, and tunability of electrical and optical properties through modification of chemical composition [8, 9].

Preliminary proof-of-concept experiments involving organic PR composites have shown great potential for use in the elimination of phase aberrations. Specifically, an organic PR composite, acting as a phase-conjugate mirror, has been used in the elimination of phase aberrations in an optical beam [3]. However, the geometry used in this demonstration precludes it from being used to transmit a signal from a sender to a receiver at a remote location. Here, an optical signal originating at the sender was passed through an aberrating medium, and subsequently, the phase-conjugate signal was redirected back to the sender through the original aberrating medium. More recently, an optical system based on a forward degenerate four-wave mixing (DFWM) geometry in which the signal was sent from

---

Electronic supplementary material The online version of this article (doi:10.1007/s00340-017-6641-y) contains supplementary material, which is available to authorized users.

✉ Jeffrey G. Winiarz
winiarzj@mst.edu

Yichen Liang
ylnq6@mst.edu

[1] Department of Chemistry, Missouri University of Science and Technology, 400W 11th Street, Rolla, MO 65409, USA

a sender to a remotely located receiver has been described [4]. It was also demonstrated that such an optical system can be used in the correction of dynamic phase aberrations [5]. Nevertheless, the geometry used in those demonstrations lacks practical applicability in that a coherent, unaberrated reference beam was required to be transmitted from the sender to the receiver. In real applications, such a requirement is impractical, because the object and reference beams (OB and RB, respectively) would be subjected to the same aberrating transmission medium. Thus, any aberration arising in the OB would also be present in the RB.

To overcome these shortcomings, a novel optical system detailed schematically in Fig. 1 is introduced. As shown in the figure, previously unrealized practical applicability is achieved in that this configuration is comprised of distinct sender and receiver, separated by an aberrating medium traversed by a single optical beam. In this model, an optical signal is encoded in a laser beam by the sender. This information is subsequently transmitted through an aberrating medium, represented in the figure by AB, which has the effect of degrading the phase quality of the encoded information. Here, the aberrating medium was fabricated by spreading epoxy across a microscope slide. Finally, the aberrated information-carrying beam reaches the receiver, where the information can be reconstructed, free of aberrations, using the optical system described herein in conjunction with a suitable PR device.

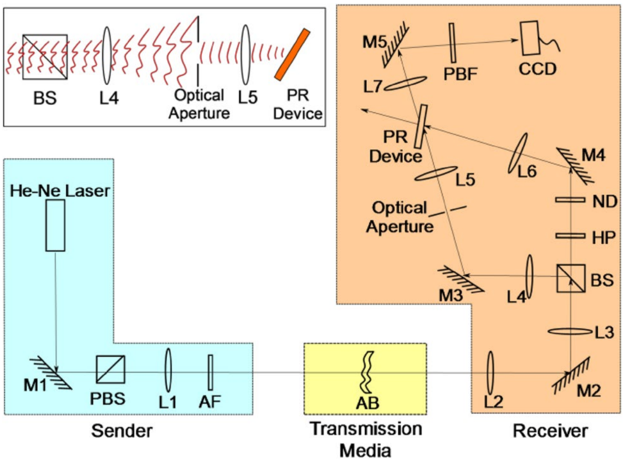

Fig. 1 Schematic diagram depicting the optical system. M denotes mirror. The *numbers in the parentheses* indicate the distance (cm) of each component from the PR device as measured along the relevant beam path. Laser (−224); M1 (−179); PBS (−161); L1 (−76), $f=25$ cm; AF (−68); AB (−67); L2 (−62), $f=7.5$ cm; M2 (−58); L3 (−52) $f=7.5$ cm; BS (−46.5); L4 (−37), $f=5$ cm; HP (−43); ND (−40.5); M3 (−32); M4 (−32.5); optical aperture (−21); L5 (−15), $f=15$ cm; L6 (−16), $f=10$ cm; L7 (15.5), $f=10$ cm; M5 (27); PBF (40); CCD (45). The *inset* illustrates the mechanism of reducing the aberrations associated with RB

2 Experimental method

An He–Ne laser operating at a wavelength of 633 nm with *s*-polarization (500:1) was used for all experiments. A polarizing beam splitter (PBS) further filtered any *p*-polarization. The beam diameter at the object, an Air Force resolution target (AF) in this case, was adjusted with lens 1 (L1). Here, the 0.5 mm sized figures from the AF were imaged (see Fig. S1 in Supplementary Material). L2, L3, and L6 were used to adjust the size of the beam at the respective optical components. The signal beam was divided into OB and RB using a 50:50 beam splitter (BS). The polarization of OB could be continuously rotated by an angle, φ, away from *s*-polarization ($\phi=0°$ is maximized *s*-polarization, and $\phi=90°$ is maximized *p*-polarization) via a half-wave plate (HP). A neutral-density filter (ND) was used to adjust the intensity of OB. To produce an RB which was relatively free of aberrations, RB was first expanded using L4 to a diameter of ~3 mm and subsequently passed through an optical aperture with a diameter of ~1 mm, allowing for a relatively "clean" portion of RB to be isolated. A schematic of this process is shown in the inset of Fig. 1. The diameter of RB at the PR device was finally adjusted using L5. For all experiments herein, OB and RB had beam areas of 0.12 cm^2 and intensities of 14.7 and 7.3 mW/cm^2, respectively, at the PR device, unless otherwise noted. The writing beams, OB and RB, intersected at an angle of 35° in the air at the PR device. The angle between the PR device normal and the beam bisector was 40°. These angles were experimentally determined to optimize the quality of the restored image. A polarizing beam filter (PBF) was placed after the PR device at the position, as indicated in Fig. 1, allowing only the *p*-polarized portion of OB, diffracted by the PR grating, to pass and subsequently be imaged by the CCD camera. Hence, the diffracted, *p*-polarized portion of OB is referred to as the information beam (IB). L7 was used to create an image plane at the CCD. Photos of the experimental setup can be found in Figs. S2 and S3 in the Supplementary Materials.

The PR composite used in this study was composed of *N,N*′-bis(3-methylphenyl)-*N,N*′-diphenylbenzidine (TPD), poly(9-vinylcarbazole) (PVK), 4-homopiperidinobenzylidenemalononitrile (7-DCST) and C_{60} with TPD:PVK:7-DCST:C_{60}=45:10:45:1.0 wt%. 7-DCST and C_{60} served as the non-linear optical chromophore and photosensitizer, respectively. A small amount of PVK was included in the composite to enhance its resistance to phase separation, as well as to decrease the dark conductivity. PR composites found in previous studies have often relied on PVK as the charge-transport species [4, 5]. More recently, however, polymers containing TPD pendant functional groups, such as poly(acrylic tetraphenyldiaminobiphenol) (PATPD), have been shown to possess superior functionality [10–12].

Specifically, the hole mobility of PATPD has been shown to be ~100 times greater than that of PVK with $E = 16$ V/µm [10]. A faster charge-carrier mobility is advantageous in PR composites, especially when response time is of concern. In addition, PR devices based on PATPD have shown improved stability in their PR performance [11, 12]. Considering the pendant geometry of the TPD groups in PATPD, it is not surprising that the polymer and the TPD monomer have similar energy gaps, E_g, between the highest unoccupied molecular orbital and the lowest occupied molecular orbital, with that of TPD being $E_g = 3.20$ eV and PATPD exhibiting $E_g = 3.23$ eV [12, 13]. Despite the monomeric nature of the TPD used in this study, the PR devices have not exhibited detectable phase separation in over 1 year. In addition, due to the predominantly molecular nature of the PR composite, the inclusion of a plasticizer was unnecessary, further increasing the available volume for functional entities within the composite [14, 15]. The PR device was fabricated by melting and sandwiching the composite between two glass slides coated with indium tin oxide to provide electrodes. The thickness of the PR devices was maintained at $d = 50$ µm using glass beads.

3 Results and discussion

As mentioned above, OB was linearly polarized and could be rotated via HP, such that it contained both *s*- and *p*-polarization. Because the other writing beam, RB, was *s*-polarized, a degree of *s*-polarization was required in OB to create the required optical interference pattern within the PR device. The *p*-polarized component was necessary to serve as a source for IB. To optimize φ, the intensity of IB was monitored as the polarization of OB was rotated and this dependence is illustrated in Fig. 2a (externally applied electric field, $E = 70$ V/µm, AF was removed, and the CCD camera was replaced by a photodiode). Evident in the figure, the intensity of IB was maximized for $\varphi = 45°$, and therefore, this φ was used in all imaging experiments. The intensity of IB was also characterized as a function of E, and the result is illustrated in Fig. 2b ($\varphi = 45°$). The maximum intensity of IB occurred at the highest applied field of $E = 70$ V/µm, and over-modulation was not observed for the range of E used in this study. Based on these results, $E = 70$ V/µm for all imaging experiments unless otherwise noted.

To gauge the imaging capability of the optical system, as shown in Fig. 1, an unaberrated image was recorded and is shown in Fig. 3a. To obtain this image, the PR device was replaced by a mirror and AB was removed. Evident from the figure, the optical system is capable of producing a clear image. Furthermore, this image serves as a control to which subsequent images can be compared. Removing the mirror and reinserting the PR device, with AB removed, yielded the image, as shown in Fig. 3b. In comparing Fig. 3a, b, it is apparent that insertion of the PR device results in a small degree of image degradation. This degradation is attributed primarily to macro- and micro-scale inhomogenialities which likely manifest in the PR composite. To minimize this effect, the PR devices were fabricated with thickness, d, of 50 µm. This thickness, while relatively thin, ensures that the PR grating is in the Bragg regime, which was confirmed through the observation of a single detectable order of diffraction [9]. The aberrated image shown in Fig. 3c was acquired by replacing the PR device with a mirror and inserting the AB at the position, as indicated in Fig. 1. As shown in the figure, the image is significantly aberrated. Finally, a corrected image shown in Fig. 3d was acquired using all the components, as shown in Fig. 1. The quality of the corrected image in Fig. 3d is nearly identical to the unaberrated image, as shown in Fig. 3b, demonstrating the ability to largely eliminate phase aberrations in the optical beam. Furthermore, the experimental geometry in Fig. 1, in conjunction with the PR composite utilized herein, was shown capable of eliminating phase aberrations in an OB conveying dynamically updating images, as shown in Video 1 of the Supplementary Material. Here, the position of the AF was oscillated back and forth with a speed of 1 mm/s in a direction perpendicular to the incident laser beam. As shown in the video, the dynamically oscillating image can be clearly identified. This stands in contrast to

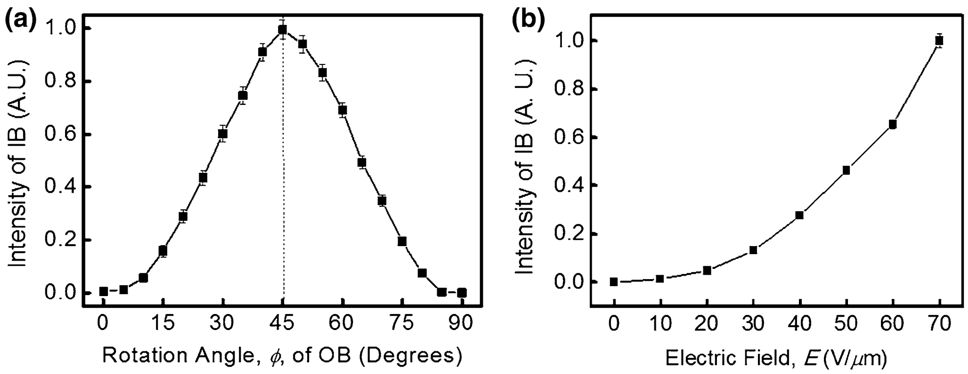

Fig. 2 Characterization of the optical system shown in Fig. 1. **a** Intensity of IB as a function of polarization rotation angle, φ, of OB. **b** Intensity of IB as a function of external electric field, E

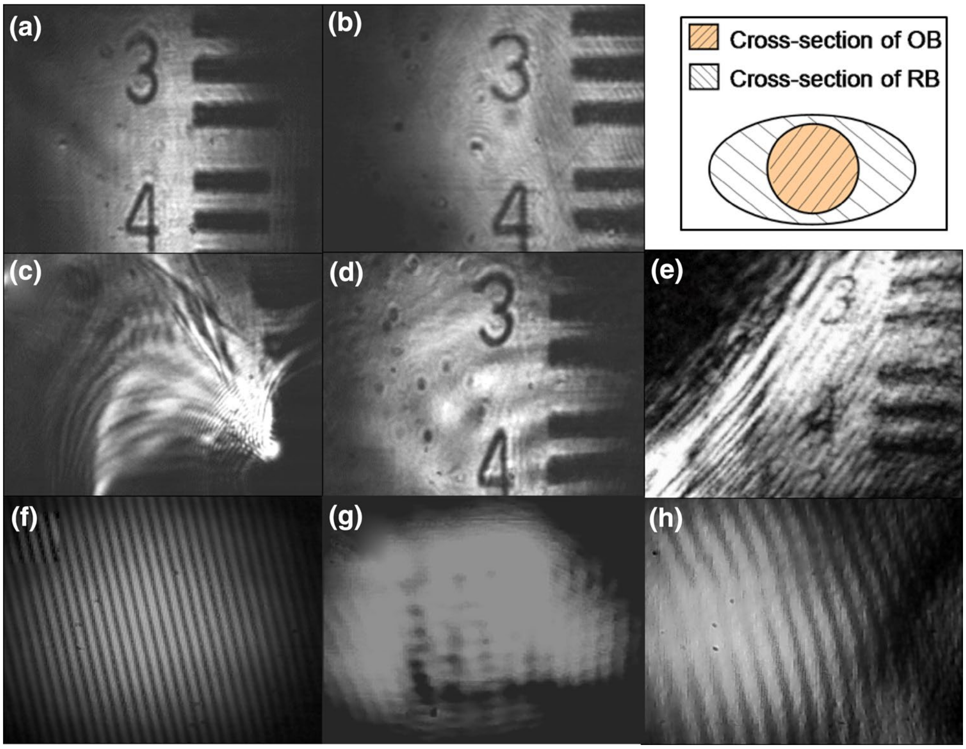

Fig. 3 **a** Unaberrated image using a mirror in place of the PR device. **b** Unaberrated image captured using the PR device. **c** Aberrated image. **d** Corrected image. **e** Corrected image captured with the optical aperture removed. **f** Interference pattern written by intersecting a coherent, plane-wave, beam with the RB between the PBS and L1. **g** Interference pattern written by intersecting a coherent, plane-wave, beam with the RB between M3 and the optical aperture (AF removed). **h** Interference pattern written by intersecting a coherent, plane-wave, beam with the RB between the optical aperture and L5 (AF removed). The *inset* depicts the configuration of the beam cross sections of OB and RB at the PR device

Video 2 in the Supplementary Material, captured by replacing the PR device with a mirror. As shown in the video, absent the corrective function of the PR device, the image is mostly unidentifiable.

The unaberrated RB was obtained using an optical aperture [16], the position and size of which greatly influenced the ability to restore the image to an unaberrated condition. Reducing the size of the aperture yielded a clearer image, however, at the expense of intensity of IB. It was determined that, under the current experimental conditions, an aperture diameter of ~1 mm yielded an optimal image. For practical applications, the aperture position and size can be adjusted using a feedback system [17]. To demonstrate the necessity of the optical aperture, an image was obtained with the aperture removed and is shown in Fig. 3e. Apparent from the figure is that the image quality decreased dramatically from that shown in Fig. 3b. Nevertheless, some degree of correction is observed in comparing Fig. 3e to the aberrated image, Fig. 3c. This is attributed to the formation of an effective optical aperture associated with the intersection of OB and RB at the PR device. As illustrated in the inset of Fig. 3, when the optical aperture was removed, the size of RB became larger than that of OB at their intersection at the PR device. Because only the portion of RB which was coincident with OB at the PR device could contribute to the PR grating, those aberrations associated with regions of RB which were not coincident with OB were essentially eliminated. Moreover, the beam cross section of RB at the PR device was "stretched" horizontally due to the relatively large incident angle of 57.5°, as compared to 22.5° for the OB. Hence, an artificial aperture was created in the region, where interference occurs, effectively reducing the aberrations associated with RB.

To characterize the spatial coherence of RB before and after passing through the aberrator and the subsequent optical aperture, interference patterns created by the intersection of RB with a coherent, plane-wave, beam were obtained. Shown in Fig. 3f is the interference pattern obtained at a position between the PBS and L1 and is included to gauge the spatial coherence of the laser beam prior to any aberrations. Evident from the figure is the familiar pattern associated with the interference of two plane waves. The interference pattern obtained after aberration of the RB, between M3 and the optical aperture (AF removed), is shown in Fig. 3g. Here, the lack of any discernable interference pattern reflects the severely aberrated nature of the RB. Finally, Fig. 3h shows the interference pattern written after the optical aperture, between the optical aperture and L5 (AF removed). Evident from this series of figures, the use of the optical aperture is effective in the restoration of the RB to a plane wave.

The elimination of phase aberrations is rooted in the holographic nature of the PR device. This process is illustrated by the equation:

$$(\Psi_{\mathrm{AB}} \cdot U_{\mathrm{OB}} + U_{\mathrm{RB}})^2 = I_{\mathrm{OB}} + I_{\mathrm{RB}} + U_{\mathrm{RB}} \cdot {U_{\mathrm{OB}}}^* \cdot {\Psi_{\mathrm{AB}}}^* + U_{\mathrm{OB}} \cdot {U_{\mathrm{RB}}}^* \cdot \Psi_{\mathrm{AB}}, \tag{1}$$

where U_{OB} and U_{RB} are the amplitudes of OB and RB, respectively, I_{OB} and I_{RB} are the intensities of OB and RB, respectively, $U_{OB}{}^{*}$ and $U_{RB}{}^{*}$ are the complex conjugates of OB and RB, respectively, and Ψ_{AB} and $\Psi_{AB}{}^{*}$ represent the phase aberrations and its complex conjugate, respectively. Here, because an aberrated OB, $\Psi_{AB}U_{OB}$, is used to write the PR grating, and assuming RB is an unaberrated plane wave, the aberrations are "encoded" in the grating. In a self-induced grating, the PR grating in this case, the grating created by the aberrated OB, $\Psi_{AB}U_{OB}$, is also read by $\Psi_{AB}U_{OB}$. Evident in the second term of the equation:

$$\begin{aligned}\Psi_{AB} \cdot U_{OB} \cdot (I_{OB} + I_{RB} + U_{RB} \cdot U_{OB}{}^{*} \cdot \Psi_{AB}{}^{*} + U_{OB} \cdot U_{RB}{}^{*} \cdot \Psi_{AB}) \\ = \left(I_{OB} + I_{RB}\right) \cdot \Psi_{AB} \cdot U_{OB} + I_{OB} \cdot U_{RB} + \left(U_{OB} \cdot U_{RB}{}^{*} \cdot \Psi_{AB}\right) \cdot \Psi_{AB} \cdot U_{OB},\end{aligned} \tag{2}$$

is that the aberrations, Ψ_{AB}, in the reading OB, $\Psi_{AB}U_{OB}$, and the complex conjugate of the phase aberrations, $\Psi_{AB}{}^{*}$, encoded in the grating, cancel each other, so that the optical beam diffracted by the grating, including IB, is aberration-free [4, 5]. A more detailed explanation can be found in the literature [18].

To confirm the PR nature of the devices used in this work, two-beam coupling (TBC) techniques were employed using the experimental setup shown in Fig. 1 with minor modifications. Specifically, PBS, AF, AB, and HP were removed and OB and RB were *p*-polarized. Bias was applied to the PR device, such that RB would experience gain at the expense of OB, and the beam intensity was monitored using a photodiode. The TBC gain coefficients are shown in Fig. 4 as a function of E and were calculated according to the equation:

$$\Gamma = [\ln(\gamma\beta) - \ln(\beta + 1 - \gamma)]/L, \tag{3}$$

where γ is the ratio of the intensity of the beam experiencing gain with and without the pump beam, β is the ratio of the writing beam intensities before the PR device, and L is the optical path length of the beam experiencing gain inside the device. For applications involving TBC-based amplifications, the net gain factor, Γ_{net}, defined as $\Gamma_{net} = \Gamma - \alpha$, should be considered. Here, α is the optical attenuation experienced by the beam as it traverses the PR device, with $\alpha = [\log(I_{RB}'/I_{RB}'')]/d = 40.82\ \mathrm{cm}^{-1}$, where I_{RB}' and I_{RB}'' are the intensities of RB before and after the PR device, respectively. Evident from Fig. 4, net gain occurs under the current experimental conditions for $E > 40$ V/μm.

To further characterize the utility of the current PR composite for future application in the current optical system, DFWM experiments were performed. As with the TBC experiments, AF, AB, and HP were removed. In this case, OB and RB were *s*-polarized, and had equal intensities of 12.12 mW/cm^2 at the PR device (adjusted using ND and removing the optical aperture). A *p*-polarized probe beam with an intensity of 0.06 mW/cm^2 and a beam area of 0.12 cm^2 were made to counter propagate opposite to OB. The diffracted probe beam was collected using a PBS located between L5 and the PR device. The internal and external diffraction efficiencies, η_{int} and η_{ext}, respectively, were measured as a function of E with the results, as shown in Fig. 5. The efficiencies were calculated using the equations $\eta_{int} = I_d/(I_d + I_t)$ and $\eta_{ext} = I_d/I_p$, in which I_p is the intensity of the probe beam before the PR device, and I_d and I_t are the intensities of the diffracted and transmitted probe beams, respectively, after the PR device. As shown in the figure, a maximum of $\eta_{int} = 10\%$ and $\eta_{ext} = 6\%$ were measured at $E = 70$ V/μm and over-modulation was not observed for the range of E used in this study. While these

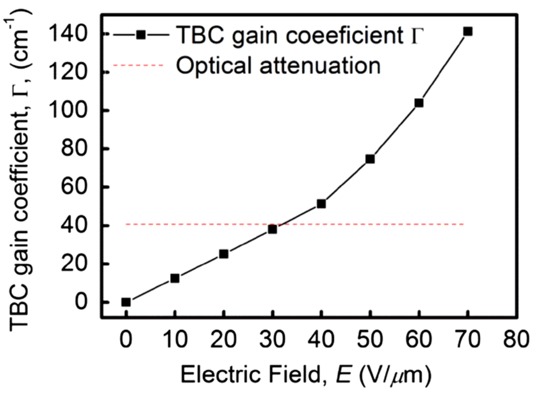

Fig. 4 TBC gain coefficient, Γ, as a function of external electric field, *E*

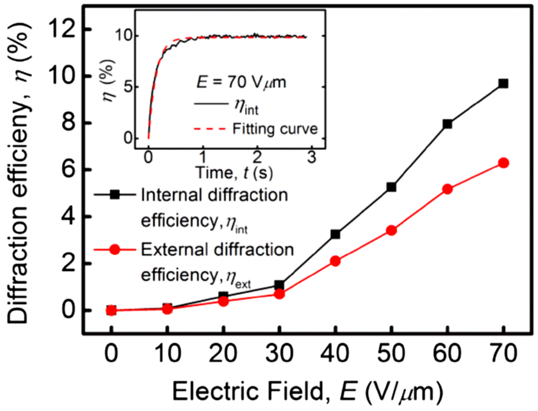

Fig. 5 Diffraction efficiencies, η, as a function of external electric field, *E*. The *inset* depicts the internal diffraction efficiency as a function of time with $E = 70$ V/μm

η are relatively low, it is noted that the optical system was optimized for image acquisition. For example, the 40° tilt angle between the PR device normal and the writing beam bisector, while optimized for image reconstruction, dictates that only a small component of E coincides with the grating vector. In addition, beam cross sections were maximized at the PR device in an effort to minimize image distortions. This resulted in beam intensities which were lower than ideal in terms of efficiency [19–21].

Time-resolved DFWM experiments were also conducted to characterize the PR grating growth rate, τ_g, under the current experimental conditions. By fitting the obtained data to the equation,

$$\eta = A\left[1 - \exp\left(-t/\tau_g\right)\right], \tag{4}$$

where A is a fitting constant [4, 22], τ_g were determined as 1.77, 0.63 and 0.28 s for $E=50$, 60 and 70 V/μm, respectively. The inset of Fig. 5 shows the time-dependent η_{int} with $E=70$ V/μm. To the best of our knowledge, this is among the fastest τ_g recorded for any PR device operating in an image correction system [3–7]. In this case, the improvement in τ_g can likely be attributed largely to the superior charge-carrier mobility of TPD, which allows for faster formation of the space-charge field. In contrast, the PVK-based PR device exhibited a maximum τ_g of 9.3 s under similar experimental conditions. The faster τ_g implies that TPD-based PR composites are well-suited for applications involving the dynamic processing of optical information [23].

4 Conclusion

In summary, a novel optical system employing a TPD-based PR composite for the elimination of phase aberrations is introduced. The optical system has the ability to restore an aberrated, information-carrying, optical beam to a nearly unaberrated condition under both static and dynamic conditions, while its potential for application in optical signal transmission is clearly established by the sender-media-receiver geometry. In addition, we demonstrate that the system has the ability to dynamically correct aberrations. The PR composite shows a net TBC gain for $E>40$ V/μm, and $\eta_{\text{int}}=6\%$ and $\eta_{\text{ext}}=10\%$ are measured with the current optical system. Moreover, with $\tau_g=0.28$ s, the TPD-based PR composite demonstrates potential for real-time image correction applications, which is the focus of future research.

Acknowledgements The authors wish to acknowledge the Materials Research Center at the Missouri University of Science and Technology, the Department of Chemistry at the Missouri University of Science and Technology, and the Missouri Research Board.

References

1. S. Niu, J. Shen, C. Liang, Y. Zhang, B. Li, Appl. Opt **50**, 4365 (2011)
2. K. Baskaran, R. Rosen, P. Lewis, P. Unsbo, J. Gustafsson, Optom. Vis. Sci **89**, 1417 (2012)
3. G. Li, M. Eralp, J. Thomas, S. Tay, A. Schulzgen, R.A. Norwood, N. Peyghambarian. Appl. Phys. Lett **86**, 161103 (2005)
4. J. Winiarz, F. Ghebremichael, Appl. Opt **43**, 3166 (2004)
5. J. Winiarz, F. Ghebremichael, Opt. Express **12**, 2517 (2004)
6. A. Chiou, P. Yeh, Opt. Lett **10**, 621 (1985)
7. A. Chiou, P. Yeh, Opt. Lett **11**, 461 (1986)
8. S. Ducharme, J. Scott, R. Twieg, W.E. Moerner, Phys. Rev. Lett **66**, 1846 (1991)
9. S. Köber, M. Salvador, K. Meerholz, Adv. Mater **23**, 4725 (2011)
10. K. Ogino, T. Nomura, T. Shichi, S. Park, H. Sato, Chem. Mater **9**, 2768 (1997)
11. J. Thomas, R.A. Norwood, N. Peyghambarian, J. Mater. Chem **19**, 7476 (2009)
12. J. Thomas, C. Fuentes-Hernandez, M. Yamamoto, K. Camnack, K. Matsumoto, G. Walker, S. Barlow, B. Kippelen, G. Meredith, S. Marder. Adv. Mater **16**, 2032 (2004)
13. P.K. Nayak, N. Agarwal, N. Periasamy, M.P. Patankar, K.L. Narasimhan. Synth. Met **160**, 722 (2010)
14. W.E. Moerner, S. Silence, F. Hache, G. Bjorklund. J. Opt. Soc. Am. B **11**, 320 (1994)
15. Y. Liang, J. Moon, R. Mu, J.G. Winiarz. J. Mater. Chem **3**, 4134 (2015)
16. M.A. Lediju, G.E. Trahey, B.C. Byram, B.J. Dahl, IEEE Trans. Ultrason. Ferroelect. FrEq. Control **58**, 1377 (2011)
17. V. Lemberg, U.S. Patent 6793654 B2, Sep 21, (2004)
18. J. W. Goodman: introduction to Fourier optics. 2nd edn. (McGraw-Hill, San Francisco 1996)
19. K. Meerholz, B.L. Volodin, B. Sandalphon, Kippelen, A. N. Peyghambarian. Nature **371**, 497 (1994)
20. V. Herrera-Ambriz, J. Maldonado, M. Rodriguez, R. Castro-Beltran, G. Ramos-Ortiz, N. Magana-Vergara, M. Meneses-Nava, O. Barbosa-Garcia, R. Santillan, N. Farfan, F. Dang, P.G. Lacroix, I. Ledoux-Rak. J. Phys. Chem. C **115**, 23955 (2011)
21. J. Moon, Y. Liang, T.E. Stevens, T.C. Monson, D.L. Huber, B.D. Mahala, J.G. Winiarz, J. Phys. Chem. C **119**(24), 13827 (2015)
22. W.E. Moerner, S.M. Silence, Chem. Rev **94**, 127 (1994)
23. D.R. Iskander, M.J. Collins, M.R. Morelande, M. Zhu, IEEE Trans. Biomed. Eng **11**, 1969 (2004)